



## Revealing the $\text{ZrO}_2$ crystal effect of Pd/ $\text{ZrO}_2$ catalyst for toluene combustion: A combined DRIFTS and DFT study

Decun Luo<sup>a</sup>, Ziyu Tang<sup>a</sup>, Xiyang Yu<sup>a</sup>, Tao Zhang<sup>a</sup>, Chun-Ran Chang<sup>a,b</sup>, Zhun Hu<sup>a,\*</sup>

<sup>a</sup> Institute of Industrial Catalysis, School of Chemical Engineering and Technology, Xi'an Jiaotong University, Xi'an, Shaanxi 710049, China

<sup>b</sup> Shaanxi Key Laboratory of Low Metamorphic Coal Clean Utilization, School of Chemistry and Chemical Engineering, Yulin University, Yulin 719000, China



### ARTICLE INFO

**Keywords:**  
 Toluene combustion  
 Pd/ $\text{ZrO}_2$   
 Crystalline form  
 DFT  
*In situ*-DRIFTS

### ABSTRACT

The effect of  $\text{ZrO}_2$  crystalline phases on Pd/ $\text{ZrO}_2$  for catalytic combustion of toluene was investigated. It was found that Pd/t-ZrO<sub>2</sub> showed superior activity when the toluene concentration was lower than 2000 ppm, while Pd/m-ZrO<sub>2</sub> performed better with toluene concentration higher than 3000 ppm. Kinetic studies showed that the reaction order of toluene on Pd/t-ZrO<sub>2</sub> and Pd/m-ZrO<sub>2</sub> is 0 and 2, respectively. The catalytic activity was controlled by combined effect of PdO activity and quantity, which was correlated with the interaction between palladium and zirconia. The t-ZrO<sub>2</sub> increased PdO species activity, while m-ZrO<sub>2</sub> could enhance the amount of PdO. DFT results showed that the p-band center of the O of PdO on t-ZrO<sub>2</sub> was higher, suggesting that PdO was more active. *In situ*-DRIFTS revealed that the reaction pathway of catalytic oxidation of toluene on Pd/ $\text{ZrO}_2$  was as follows: toluene was oxidized stepwise to benzyl alcohol, benzaldehyde, benzoic acid, CO<sub>2</sub> and H<sub>2</sub>O.

### 1. Introduction

VOCs (Volatile Organic Compounds) refer to a variety of organic compounds that are gaseous at room temperature, with the boiling points of 50–260 °C, which could result in ozone depletion and photochemical smoke that were harmful to human health and crop growth [1]. Many strategies have been devoted to eliminating VOCs. The catalytic combustion technology was regarded as one of the most promising methods because of its simplicity, secure, low energy consumption and high efficiency [2–8]. Extensive attention has been paid to Pd-based [9–15] catalysts for VOC combustion, mainly because Pd plays a dual role in the reaction processes: Pd site is active for the decomposition of VOCs and Pd oxide provides the surface oxygen source of the catalyst.

Supports, in supported Pd-based catalysts, as key components of catalysts, not only play an important role in the dispersion of the active sites, but also modify the catalytic activity via tuning the interaction between active sites and supports, etc. [12,16–20]. The roles of support on the Pd-based catalysts have been extensively studied, i.e., CeO<sub>2</sub> [21–24], SiO<sub>2</sub> [20,25,26], Al<sub>2</sub>O<sub>3</sub> [27,28] and ZrO<sub>2</sub> [29–34]. Miller et al. [32] found the catalytic activity of the supported Pd-based catalyst for methane oxidation. The activity of the catalysts depended on the amount of PdO–oxygen vacancy (Pd), which was in relation to the stability of PdO. The order of catalytic activity was Pd/Al<sub>2</sub>O<sub>3</sub> >

Pd/ZrO<sub>2</sub>–CeO<sub>2</sub> > Pd/CeO<sub>2</sub>, which was consistent with the weak interaction between palladium and supports (Al<sub>2</sub>O<sub>3</sub> < ZrO<sub>2</sub>–CeO<sub>2</sub> < CeO<sub>2</sub>). Meanwhile, supports could also influence the mechanical stability, resistance to toxicity and hydrothermal stability of the catalysts [35]. Araya et al. discovered that Pd/ZrO<sub>2</sub> catalyst showed higher water-resistance than Pd/SiO<sub>2</sub> catalyst [36]. Similar results were also reported by Park et al. [33]. They found that Pd/ZrO<sub>2</sub> catalysts exhibited higher activity and better stability in the presence of water vapor compared with Pd/Al<sub>2</sub>O<sub>3</sub>. Compared with other supports in Pd-based catalysts, from a practical point of view, ZrO<sub>2</sub> was regarded as a promising carrier for further application.

The textural properties, acidity, and crystal structures of ZrO<sub>2</sub> will affect the catalytic performance. Shin et al. [31] found that lower surface area of ZrO<sub>2</sub> in Pd/ZrO<sub>2</sub> catalysts could induce the formation of larger PdO particles, which showed higher activity than small PdO particles. Zhang et al. [29] prepared ZrO<sub>2</sub> with different crystallinities by pyrolysis of UiO-66 at distinct temperatures for catalytic oxidation of CO. The higher activity was related to the higher ratio of O<sub>ads</sub>/O<sub>lat</sub> species and Pd<sup>0</sup>/Pd<sup>2+</sup> on Pd/ZrO<sub>2</sub> catalysts, which was in relation to the proportion of tetragonal /monoclinic phase in mixed crystalline phases. Zheng et al. [34] studied the effect of crystal forms of ZrO<sub>2</sub> on the hydrodechlorination of chlorobenzene. They found that the catalytic performance of Pd/m-ZrO<sub>2</sub> was better than Pd/t-ZrO<sub>2</sub>, which was owing

\* Corresponding author.

E-mail address: [huzhun@mail.xjtu.edu.cn](mailto:huzhun@mail.xjtu.edu.cn) (Z. Hu).

to higher dispersion and content of Pd species that led to stronger interaction between metal and support. However, only few studies were reported on the effect of crystal phases of  $\text{ZrO}_2$  on  $\text{Pd}/\text{ZrO}_2$  for the catalytic combustion of VOCs.

In this study, we investigated the differences in the performance of  $\text{Pd}/\text{ZrO}_2$  catalysts with different crystalline of  $\text{ZrO}_2$  for toluene catalytic combustion. To gain insights into the structure-performance relationship in the catalysts, the kinetic studies, surface properties (XPS and  $\text{H}_2$ -TPR), and DRIFTS were used to understand the effects of  $\text{ZrO}_2$  crystalline on  $\text{Pd}/\text{ZrO}_2$  for toluene combustion.

## 2. Experimental

### 2.1. Chemicals

The chemical reagents used in the experiment were purchased from Aladdin Chemical and Energy Chemical, and the chemical purity was Analytical Reagent.

### 2.2. Catalyst preparation

Zirconia with different crystal phases (tetragonal zirconia and monoclinic zirconia) were synthesized by hydrothermal method [37]. Typically, zirconium nitrate and urea were first dissolved in deionized water to form 50 mL aqueous solution ( $[\text{Zr}] = 0.4 \text{ mol/L}$ , [urea]:  $[\text{Zr}] = 10: 1$ ). The solution was then introduced to a 100 mL self-pressurized stainless steel hydrothermal kettle lined with Teflon, and then placed in an oven at 200 °C for 6 h. The resultant solid was washed by centrifugation with deionized water for 1–3 times until the supernatant was neutral. The obtained material after centrifugation was dried in an oven at 110 °C overnight, and then calcined at 400 °C for 4 h. The obtained powder was denoted as m- $\text{ZrO}_2$ . Tetragonal zirconia (t- $\text{ZrO}_2$ ) was prepared with the similar procedure as m- $\text{ZrO}_2$ , except that anhydrous methanol was dissolved zirconium nitrate and urea instead of water.

$\text{Pd}/\text{ZrO}_2$  was prepared via wet impregnation method. Typically, 0.99 g  $\text{ZrO}_2$  (m- $\text{ZrO}_2$  or t- $\text{ZrO}_2$ ) was added in 20 mL  $\text{H}_2\text{O}$ . Then 1 mL  $\text{Pd}(\text{NO}_3)_2$  aqueous solution (10 mg  $\text{Pd}/\text{mL}$ ) was added into the solution with vigorous stirring for 24 h at room temperature. The solvent was removed by a rotary evaporator at 60 °C for 1 h. The resultant powder was dried overnight in an oven at 110 °C and then calcined in air at 500 °C for 6 h. The obtained samples were denoted as  $\text{Pd}/\text{m-ZrO}_2$  and  $\text{Pd}/\text{t-ZrO}_2$ .

### 2.3. Catalytic activity test

The catalytic performance and kinetic studies were measured in a U-shaped quartz tube reactor (diameter 4 mm) under toluene +  $\text{O}_2$  +  $\text{N}_2$  with different toluene and oxygen concentrations, as our previous report [38]. In a typical test, the catalyst was pretreated with 20 vol%  $\text{O}_2/\text{N}_2$  for 30 min at 400 °C. The catalyst was cooled to room temperature, and then the feed gas was introduced into the reactor. The reaction temperature was then increased from room temperature to 400 °C with a step of 10 °C and each temperature was held for 30 min to ensure that the reaction reached the steady state. The effluent gas was analyzed using a GC-7820 gas chromatograph. The formula for the toluene oxidation rate or reaction rate is as follows:

$$r = \frac{c \times X \times F}{V \times m}$$

Where  $r$ ,  $c$   $X$ ,  $F$ ,  $V$ , and  $m$  represent toluene reaction rate, toluene concentration, toluene conversion ratio, gas volume flow rate, molar volume of gas and catalyst quality, respectively.

### 2.4. Characterization of the catalysts

Transmission electron microscope (TEM) images were obtained with a Talos F200X Lorenz with an acceleration voltage of 200 kV. The measured samples were sonicated and dispersed in water, and the solution was dropped on a fine carbon film and left for 12 h at room temperature. The carbon film was then scanned and photographed. Inductively coupled plasma mass spectrometer (ICP-MS) was used to measure the content of palladium. Nitrogen adsorption and desorption isotherms were measured using a Belsorp-Max instrument. Samples were degassed in a vacuum of 200 °C for 2 h prior to measurement. The surface area was determined by Brunauer-Emmett-Teller (BET) method, and the pore size distribution was calculated by Barrett-Joyner-Halenda method. The X-ray diffraction (XRD) pattern was measured with the XRD-6100 equipment manufactured in Shimadzu, Japan, which has a maximum power of 3 kW. The scanning rate was 7°/min and the scanning range was 10–80°. X-ray photoelectron spectroscopy (XPS) was obtained with Thermo Fisher ESCALAB Xi+ equipment, using the adventitious carbon at 284.6 eV as the internal standard to calibrate the binding energy.

The oxygen storage capacity (OSC) and oxygen release rate (ORR) of the catalysts were measured using a NETZSCH-STA449F5 thermal gravimetric analyzer. Before measurement, the samples were first pretreated in a 20 %  $\text{O}_2/\text{Ar}$  atmosphere at 400 °C to remove impurities. Then the temperature was decreased to a certain temperature, the two atmospheres of 10 %  $\text{H}_2/\text{Ar}$  and 20 %  $\text{O}_2/\text{Ar}$  were switched with three or four times until the weight change remain the same.

$$\text{OSC}(\mu\text{mol/g}) = -\frac{W_{\text{oxi-red}}}{W_{\text{cat}} \times n_0}$$

$$\text{ORR}(\mu\text{mol}/(\text{g} \bullet \text{s})) = -\frac{DTG_{\text{max-red}}}{W_{\text{cat}} \times n_0}$$

Where  $W_{\text{oxi-red}}$  represents the weight differential of the catalyst under oxidative atmosphere and reductive atmosphere;  $W_{\text{cat}}$  is the mass of the catalyst when put into the crucible;  $DTG_{\text{max-red}}$  is the maximum slope of weight loss curve of catalyst in reducing atmosphere;  $n_0$  is the atomic mass of oxygen.

*In-situ* Diffuse Reflectance Infrared Fourier Transform Spectroscopy (DRIFTS) was measured with a Nicolet iS50 device to detect some intermediates or functional groups in the reaction process. DRIFTS was obtained in the range of 650–4000  $\text{cm}^{-1}$  with a resolution of 4  $\text{cm}^{-1}$  by accumulating 32 scans. The temperature was controlled by the Pike temperature module, and the raw gas was controlled by the mass flow controller. The catalyst was pretreated for 1 h in a 20 vol%  $\text{O}_2 + \text{N}_2$  (40 mL/min) stream at 400 °C, and the background spectrum was deducted in  $\text{N}_2$  stream at 150 °C. The experiment details were the same as our previously work [38].

### 2.5. Computational details

The spin-polarized density functional theory (DFT) calculations were implemented by using the Vienna ab-initio Simulation Package (VASP) [39]. Projection-augmented wave (PAW) pseudopotential was used to represent core electrons with a cutoff energy of 400 eV [40]. Perdew Burke Ernzerhof (PBE) [41] and generalized gradient approximation (GGA) were used to calculate the exchange correlation potential. Partial density of states (PDOS) curve was calculated using LOBSTER [42]. The  $7 \times 7 \times 7$  and  $8 \times 8 \times 6$   $k$ -point mesh sampling grid were used in the bulk of m- $\text{ZrO}_2$  and t- $\text{ZrO}_2$ , respectively. A  $1 \times 1 \times 1$   $k$ -point mesh sampling grid was used in the surfaces system. A monoclinic  $\text{ZrO}_2$  cell of  $5.15 \times 5.21 \times 5.31 \text{ \AA}$  and a tetragonal  $\text{ZrO}_2$  cell of  $3.64 \times 3.64 \times 3.64 \text{ \AA}$  were optimized, which were in good agreement with the experimental results [31]. The m- $\text{ZrO}_2$  (111) and t- $\text{ZrO}_2$  (101) surface systems which are the most stable surfaces of thermodynamics

were chosen to build a rhombic supercell of  $6.71 \times 7.30 \times 17.91 \text{ \AA}$  and a cuboid supercell of  $6.31 \times 7.17 \times 16.71 \text{ \AA}$ , respectively. The bottom-two atomic layers of the slab were fixed and other layers were relaxed. The vacuum space of both systems was set as  $12 \text{ \AA}$ . In order to build a suitable catalyst model, a single Pd atom was adsorbed on the top surface of  $\text{ZrO}_2$ , and an O atom was connected to the top of the Pd atom. The convergence tolerance for self-consistent field tolerance and threshold of forces on atoms are set as  $10^{-5} \text{ eV}$  and  $0.02 \text{ eV}/\text{\AA}$ , respectively.

The energy of O dissociation from O-Pd/ $\text{ZrO}_2$  system ( $E_{\text{des}}$ ) was calculated as follows.

$$E_{\text{des}} = E_{\text{Pd/ZrO}_2} - E_{\text{O-Pd/ZrO}_2} + E_0$$

where  $E_{\text{Pd/ZrO}_2}$  and  $E_{\text{O-Pd/ZrO}_2}$  are the total energy of Pd/ $\text{ZrO}_2$  system and O-Pd/ $\text{ZrO}_2$  system, respectively.  $E_0$  is total energy of  $1/2\text{O}_2$ .

For quantitative comparison, energy-weighted average  $\varepsilon$  (p-band center) was used as the descriptor of these projection bands:

$$\varepsilon = \frac{\sum \text{PDOS}(E_i) \bullet E_i}{\sum \text{PDOS}(E_i)}$$

where  $\sum \text{PDOS}(E_i)$  is the PDOS in an energy range  $[E_i, E_i + \Delta E]$  ( $\Delta E$  was a value of  $0.05 \text{ eV}$ ). For O, the sum over the highest occupied 2 s and 2p states fall into range of  $-10\text{--}0 \text{ eV}$  [42].

### 3. Results and discussion

#### 3.1. Crystalline structures and morphology

**Fig. 1A** shows the XRD patterns of Pd/m-ZrO<sub>2</sub>, m-ZrO<sub>2</sub>, Pd/t-ZrO<sub>2</sub> and t-ZrO<sub>2</sub>. All the diffraction peaks on Pd/t-ZrO<sub>2</sub> and Pd/m-ZrO<sub>2</sub> were ascribed to tetragonal zirconia (JCPDS 37-1484) and monoclinic zirconia (JCPDS 50-1089), respectively. No peak of palladium in the Pd/ $\text{ZrO}_2$  spectrum was observed, indicating that palladium did not exist on the carrier in the form of a crystal. The grain size calculated by Scherrer equation and the grain size of Pd/t-ZrO<sub>2</sub> and Pd/m-ZrO<sub>2</sub> are 5.3 and 6.9 nm, respectively.

The N<sub>2</sub> adsorption-desorption isotherms of Pd/ $\text{ZrO}_2$  and ZrO<sub>2</sub> are shown in **Fig. 1B** and **Fig. S1**, respectively. The isotherms of physical adsorption and desorption of all the catalysts can be assigned to IV isotherms with H3-type [29]. **Table 1** lists the specific surface area, average pore size and pore volume of Pd/ $\text{ZrO}_2$  catalysts. The specific surface areas of Pd/m-ZrO<sub>2</sub> and Pd/t-ZrO<sub>2</sub> are 109 and 96 m<sup>2</sup>/g, respectively. The pore volumes of Pd/m-ZrO<sub>2</sub> and Pd/t-ZrO<sub>2</sub> were 0.19 and 0.16 mL/g and the average pore sizes of Pd/m-ZrO<sub>2</sub> and Pd/t-ZrO<sub>2</sub> were 6.8 and 5.1 nm, respectively. The structures of the two mesoporous

**Table 1**  
Physicochemical parameters of the catalysts.

Catalyst	$S_{\text{BET}}$ (m <sup>2</sup> / g)	Pore volume (mL/g)	Mean pore diameter (nm)	D <sup>a</sup> (nm)	$O_{\text{ads}}/O_{\text{lat}}$ (%)	Pd <sup>2+</sup> / Pd <sup>b</sup> (%)	Pd content <sup>c</sup> (mg/g)
Pd/m- $\text{ZrO}_2$	109	0.19	6.8	6.6	14	47	10
Pd/t- $\text{ZrO}_2$	96	0.16	5.1	5.8	10	37	10

<sup>a</sup> The crystal sizes of catalysts were calculated by Scherrer equation in XRD.

<sup>b</sup> Calculated according to the corresponding peak area in XPS.

<sup>c</sup> Measured by inductively coupled plasma mass spectrometer (ICP-MS).

materials nearly identical. In addition, no difference in physical properties was found between the ZrO<sub>2</sub> support and Pd/ZrO<sub>2</sub>.

**Fig. 2** shows the TEM images of Pd/m-ZrO<sub>2</sub> and Pd/t-ZrO<sub>2</sub>. The sizes of these catalysts are 6.7 and 5.8 nm respectively. The size of the lattice fringes on Pd/m-ZrO<sub>2</sub> were 0.32, 0.28 and 0.18 nm, which corresponded to the (111), (111) and (022) of the ZrO<sub>2</sub> monoclinic crystal, respectively. Similarly, for Pd/t-ZrO<sub>2</sub>, the sizes of its lattice fringes were 0.26, 0.18 and 0.30 nm, which were ascribed to (110), (112) and (011). The EDS composition analysis diagrams of Pd/m-ZrO<sub>2</sub> and Pd/t-ZrO<sub>2</sub> indicated that Pd was distributed on the carrier ZrO<sub>2</sub> with high dispersion, which was consistent with the XRD results.

#### 3.2. Catalytic performance

The blank experiment was first carried with only quartz sand without catalysts. No measurable reaction rate was observed in the investigated reaction temperature of 100–400 °C. **Figs. 3A** and **3B** show the catalytic performance of Pd/t-ZrO<sub>2</sub> and Pd/m-ZrO<sub>2</sub> at various toluene concentrations as a function of temperature, respectively. The toluene conversion with respect to temperature shows an S-shaped curve. For Pd/t-ZrO<sub>2</sub>, the toluene conversion decreased with increasing toluene concentration. The opposite phenomenon was observed on Pd/m-ZrO<sub>2</sub>. The specific data of toluene conversion rate at different temperatures and toluene concentrations are shown in **Table S2**. At 220 °C, the oxidation rates of toluene on Pd/t-ZrO<sub>2</sub> and Pd/m-ZrO<sub>2</sub> at 1000 ppm were 29.7 and 6.6 μmol (g<sub>cat</sub> s)<sup>-1</sup>, while the oxidation rates of toluene on Pd/m-ZrO<sub>2</sub> and t-ZrO<sub>2</sub> at 4000 ppm were 25.4 and 110.6 μmol (g<sub>cat</sub> s)<sup>-1</sup>, respectively. The corresponding TOF of Pd/ZrO<sub>2</sub> is shown in **Table S3**. The oxidation rates of toluene as a function of toluene on Pd/ZrO<sub>2</sub> catalysts are shown in **Fig. 3C** and D. The activity of Pd/t-ZrO<sub>2</sub> was higher than that of Pd/m-ZrO<sub>2</sub> with a toluene concentration below 2000 ppm, on the contrary, the situation is reversed with a toluene

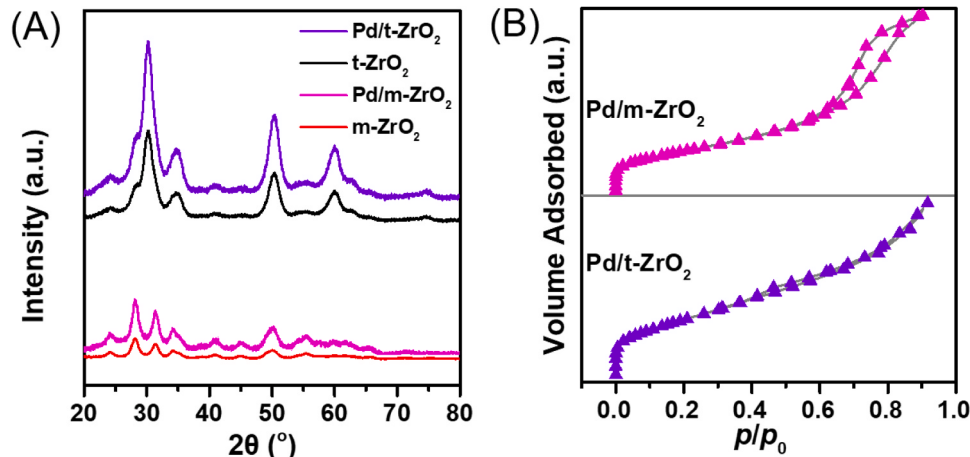


**Fig. 1.** (A) XRD patterns; (B) N<sub>2</sub> adsorption-desorption isotherm of Pd/m-ZrO<sub>2</sub> and Pd/t-ZrO<sub>2</sub>.

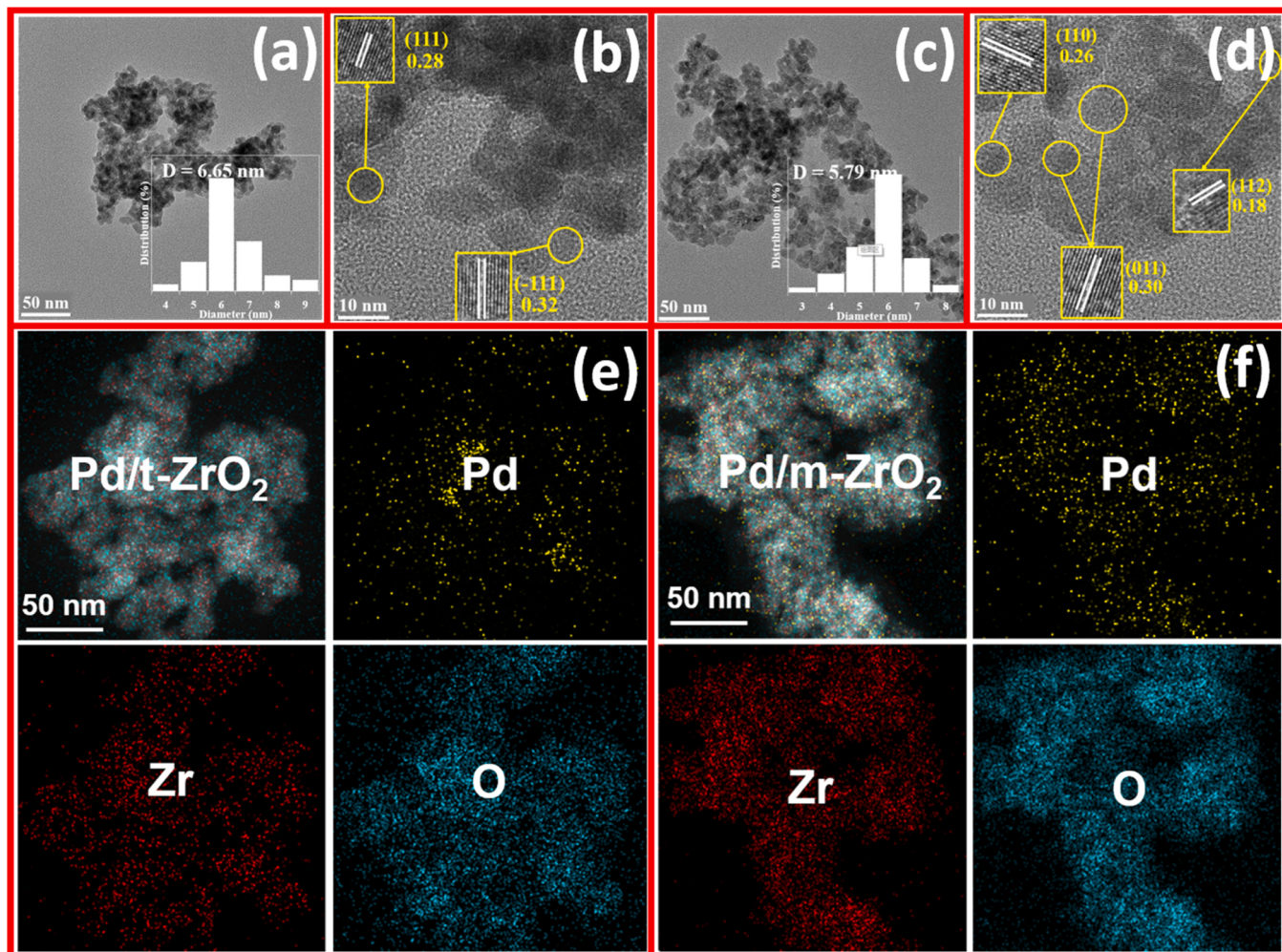


**Fig. 2.** TEM images of Pd/m-ZrO<sub>2</sub> (a) and Pd/t-ZrO<sub>2</sub> (c), HRTEM images of Pd/m-ZrO<sub>2</sub> (b) and Pd/t-ZrO<sub>2</sub> (d), EDS composition of Pd/m-ZrO<sub>2</sub> (e) and Pd/t-ZrO<sub>2</sub> (f).

concentration above 3000 ppm. Meanwhile, by calculating the apparent activation energies of Pd/m-ZrO<sub>2</sub> and Pd/t-ZrO<sub>2</sub> at different toluene concentrations (Table S4), it was found that Pd/m-ZrO<sub>2</sub> possessed the lowest activation energy (125 kJ/mol) at 4000 ppm toluene, while Pd/t-ZrO<sub>2</sub> exhibited the lowest activation energy at 1000 ppm toluene (103 kJ/mol). In addition, the cyclic test and long stabilities of catalysts are shown in Fig. S2 and Fig. S3. It was found that the two catalysts exhibited excellent stability under the all investigated reaction temperatures.

In order to understand the intrinsic activity of Pd/ZrO<sub>2</sub>, the mass specific activities with respect to toluene and oxygen concentration in the kinetic region are represented. Note that the reaction order of oxygen on both Pd/ZrO<sub>2</sub> catalysts were 0, as shown in Fig. S4. Based on the power model, the reaction equation could be expressed as follows:

$$r = kc_{(toluene)}^a$$

Where  $r$ ,  $k$ ,  $c_{(toluene)}$  and  $a$  represent toluene reaction rate, rate constant, toluene concentration and reaction order, respectively. The reaction order of toluene on Pd/t-ZrO<sub>2</sub> catalyst was almost 0. However, the reaction order of toluene on Pd/m-ZrO<sub>2</sub> catalyst was 2 at 200, 210 and 220 °C (Figs. 3C and 3D). These results indicated the key step was the toluene adsorption and activation, which resulted in the different results in catalytic activity. The different reaction orders were due to the different reaction mechanisms. The different toluene concentrations and oxygen concentrations were measured to understand the reaction mechanisms, which followed the same procedures as our previous work

[38]. But no specific mechanism could be established to illustrate all the reaction, which was probably the mixed mechanism [43,44] in the catalytic oxidation reaction. Previous references have shown that the adsorption of toluene was hinged by the redox properties of Pd [9,17]. Therefore, H<sub>2</sub>-TPR and XPS were used to characterize redox properties of the catalyst surfaces.

### 3.3. Redox properties of catalyst surface

**Fig. 4A** shows the H<sub>2</sub>-TPR curves of Pd/ZrO<sub>2</sub> and ZrO<sub>2</sub>. The ZrO<sub>2</sub> samples only contained two reductions peaks in the range of 400–600 °C. Both Pd/ZrO<sub>2</sub> samples showed one negative and four positive peaks corresponding to the reduction peaks of different oxygen species. An inverted peak was observed, which could belong to the decomposition of PdH<sub>x</sub> ( $x < 1$ ) at low temperature (100 °C). During the H<sub>2</sub>-TPR experiment, Pd first reacted with hydrogen to form palladium hydride at low temperatures [45]. As the temperature rises, the PdH<sub>x</sub> species decomposed and produced hydrogen, resulting in inverted peaks. For the positive peaks, the peak at ca. 150 °C was assigned to the reduction peaks of PdO on the catalyst surface [30,34] and the peaks near 300 °C were regarded as the reduction peaks of Pd–O–Zr species [46]. The two peaks near 400–600 °C were assigned to surface lattice oxygen and bulk phase lattice oxygen of ZrO<sub>2</sub> [29]. The reduction temperatures of PdO and Pd–O–Zr species in Pd/t-ZrO<sub>2</sub> were lower than those in Pd/m-ZrO<sub>2</sub>, which was probably in relation to the easier electron transfer from zirconia to palladium in Pd/t-ZrO<sub>2</sub>. The strong interaction between m-ZrO<sub>2</sub> and Pd, compared with Pd/t-ZrO<sub>2</sub>, resulted

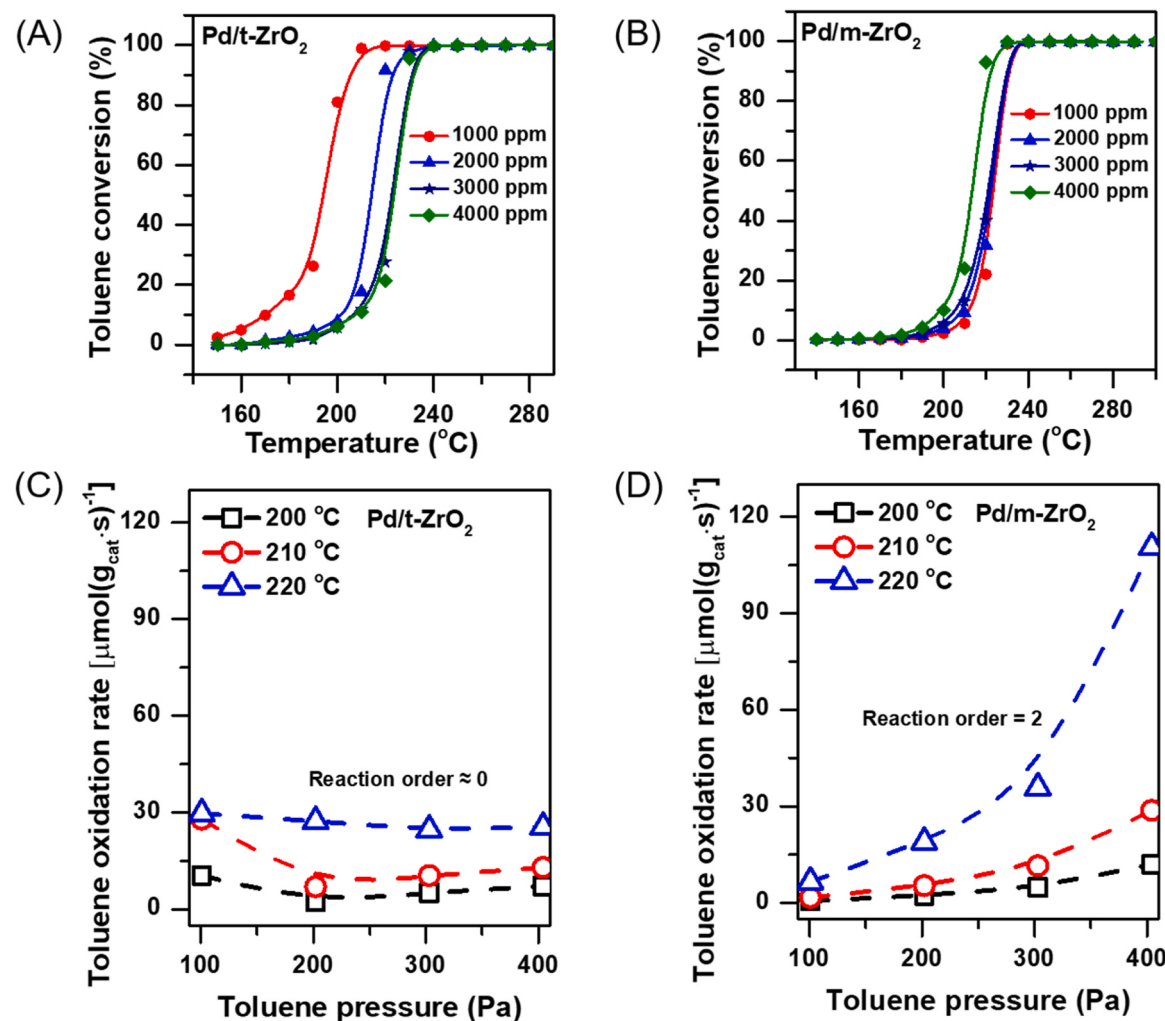


**Fig. 3.** The catalytic performance of Pd/t-ZrO<sub>2</sub> (A) and Pd/m-ZrO<sub>2</sub> (B) at different toluene concentrations as a function of the temperature; The relationship between toluene oxidation rate and toluene pressure of Pd/t-ZrO<sub>2</sub> (C) and Pd/m-ZrO<sub>2</sub> (D).

in the difficulty in the reduction of Pd–O. The area of the first peak belonging to surface PdO on Pd/m-ZrO<sub>2</sub> was 1.6 times larger than that of Pd/t-ZrO<sub>2</sub>. Meanwhile, the area of the fourth positive peak of lattice oxygen of t-ZrO<sub>2</sub> was one-fold as that of m-ZrO<sub>2</sub>, which was probably due to the migration of lattice oxygen from m-ZrO<sub>2</sub> to the Pd and the more formation of PdO species. From the results of H<sub>2</sub>-TPR, it could be concluded that t-ZrO<sub>2</sub> resulted in the formation of highly active PdO species, while m-ZrO<sub>2</sub> was beneficial to the larger amount of PdO species.

The valence states and contents of various elements on the catalyst surface were measured by XPS, and the results are shown in Fig. 4C and D. The XPS spectrum of Pd 3d and Zr 3p could be divided into six peaks (Fig. 4C), which could be ascribed to Zr 3p<sub>1/2</sub> (332.7 eV), Zr 3p<sub>3/2</sub> (346.4 eV), Pd<sup>0</sup> 3d<sub>3/2</sub> (335.5 eV), Pd<sup>0</sup> 3d<sub>5/2</sub> (341.5 eV), Pd<sup>2+</sup> 3d<sub>3/2</sub> (337.7 eV) and Pd<sup>2+</sup> 3d<sub>5/2</sub> (343.2 eV) [4,13]. The quantitative results of XPS results are shown in Table 1. The content of Pd<sup>2+</sup> in Pd/m-ZrO<sub>2</sub> (47 %) was higher than that in Pd/t-ZrO<sub>2</sub> (36 %), which was consistent with the results of H<sub>2</sub>-TPR. The higher content of Pd<sup>2+</sup> may be related to the stronger interaction between Pd and ZrO<sub>2</sub>. H<sub>2</sub>-TPR results showed that the higher reduction temperature of Pd–O–Zr on Pd/m-ZrO<sub>2</sub>, which indicated the stronger interaction between Pd and m-ZrO<sub>2</sub> on Pd/m-ZrO<sub>2</sub>. Meanwhile, the interaction between Pd and ZrO<sub>2</sub> could also affect the property of oxygen. The stronger interaction between Pd and ZrO<sub>2</sub> led to a more favorable oxidation state for Pd. Fig. 4D shows the XPS spectrum of O 1 s. Two peaks were detected at 529.9 eV and

531.8 eV, which belonged to lattice oxygen (O<sub>lat</sub>) and adsorbed oxygen (O<sub>ads</sub>) [29], respectively. The ratio of O<sub>ads</sub> to O<sub>lat</sub> is listed in Table 1. The O<sub>ads</sub>/O<sub>lat</sub> ratios of Pd/m-ZrO<sub>2</sub> and Pd/t-ZrO<sub>2</sub> are 63 % and 49 %, respectively. Both the higher Pd<sup>2+</sup>/Pd and O<sub>ads</sub>/O<sub>lat</sub> were in relation to the interaction between Pd and ZrO<sub>2</sub> [47,48]. The higher O<sub>ads</sub>/O<sub>lat</sub> ratio of Pd/m-ZrO<sub>2</sub> could be beneficial to the activation of toluene [33]. Based on our kinetic studies, the promotional effects on the toluene activation could increase the catalytic activity, since the order of toluene was 2 in Pd/m-ZrO<sub>2</sub>.

Fig. S5 shows the in-situ DRIFTS CO adsorption spectra over Pd/m-ZrO<sub>2</sub> and Pd/t-ZrO<sub>2</sub>. The two characteristic peaks between 2000 and 2200 cm<sup>-1</sup> were the linear adsorption of CO in the oxidized state Pd (CO–Pd<sup>2+</sup>) and the reduced state Pd (CO–Pd<sup>0</sup>), respectively [48]. The two characteristic peaks between 1800 and 2000 cm<sup>-1</sup> were bridge adsorption of CO in Pd<sup>0</sup> and triple hollow adsorption [49]. According to the linear adsorption of CO in the region of 2000–2200 cm<sup>-1</sup>, the areal ratio of CO–Pd<sup>2+</sup> and CO–Pd<sup>0</sup> on Pd/m-ZrO<sub>2</sub> catalyst was 0.93, which was higher than that of the Pd/t-ZrO<sub>2</sub> catalyst (0.73), and was consistent with the results of XPS.

In order to quantify the content of the surface oxygen of catalysts, oxygen storage capacity (OSC) was measured via switching H<sub>2</sub>/O<sub>2</sub> atmosphere [38]. Fig. 4B shows the TGA curves of Pd/m-ZrO<sub>2</sub> and Pd/t-ZrO<sub>2</sub> catalysts in the cycle of oxidative and reductive atmosphere. The oxygen storage capacity (OSC) of Pd/m-ZrO<sub>2</sub> was 638 μmol O/g<sub>cat</sub>, which was more than 3-fold higher than Pd/t-ZrO<sub>2</sub> (178 μmol O/g<sub>cat</sub>).

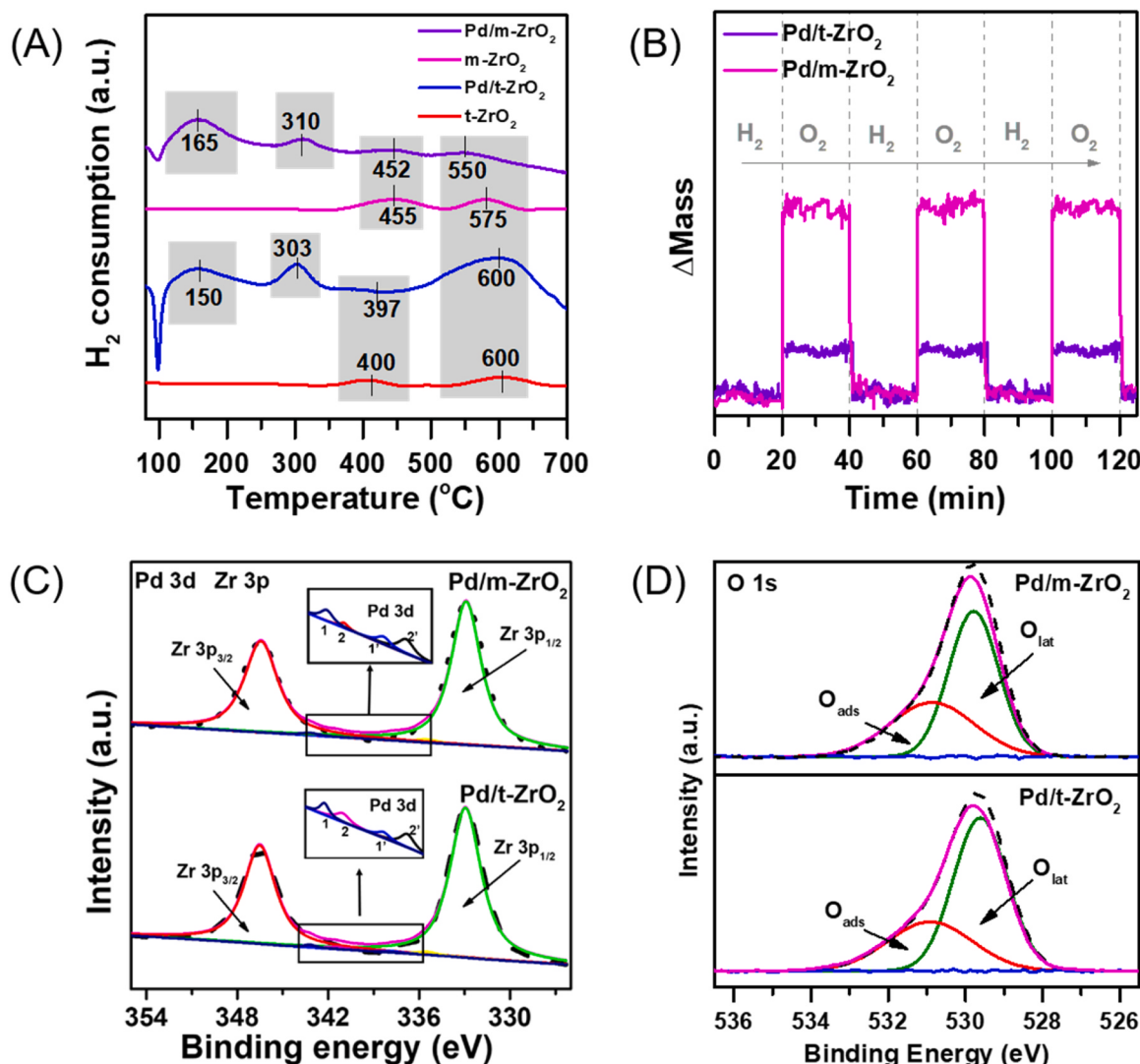


**Fig. 4.** H<sub>2</sub>-TPR curves (A); Thermogravimetric (TG) spectrogram (B) when oxygen and hydrogen were introduced alternately; XPS spectra of Pd and Zr (C) (peak of Pd<sup>2+</sup> 3d<sub>3/2</sub> O, Pd<sup>2+</sup> 3d<sub>5/2</sub> (1'), Pd<sup>0</sup> 3d<sub>3/2</sub> (2) and Pd<sup>0</sup> 3d<sub>5/2</sub> (2'')); XPS spectra of O (D).

The OSC of m-ZrO<sub>2</sub> and t-ZrO<sub>2</sub> were 595 and 141 μmol O/g<sub>cat</sub> (Fig. S6), respectively. These results indicated that the oxygen in m-ZrO<sub>2</sub>, which participated in the reaction, was more than 4-fold of that in t-ZrO<sub>2</sub>. Meanwhile, the ORR of Pd/m-ZrO<sub>2</sub> (0.53 μmol O/g<sub>cat</sub>/s) was nearly twice of Pd/t-ZrO<sub>2</sub> (0.29 μmol O/g<sub>cat</sub>/s). The large amount of oxygen migration resulted in a positive effect on the formation of active PdO<sub>x</sub> species on m-ZrO<sub>2</sub>, which enhanced the catalytic activity at the high toluene concentration.

The temperature-programmed surface reaction (TPSR) was investigated in the absence of O<sub>2</sub> (Fig. S7), and mass spectrometry was used to detect all the effluent reaction gas. Only CO<sub>2</sub> and H<sub>2</sub>O, and no other intermediates was observed. According to the results, it was concluded that the intermediates existed on the catalyst surface at an adsorbed state. In addition, the absence of O<sub>2</sub> in the TPSR results indicated that the reaction mechanism of toluene combustion over Pd/ZrO<sub>2</sub> follows the Mars-van Krevelen (MvK) mechanism. Meanwhile, it could be concluded from the amount of CO<sub>2</sub> (*m/z* = 44) over Pd/m-ZrO<sub>2</sub> that Pd/m-ZrO<sub>2</sub> contained more active oxygen species than Pd/t-ZrO<sub>2</sub> catalyst.

#### 3.4. In situ-DRIFTS

*In situ*-DRIFTS experiments were used to study the reaction pathway of toluene on the catalyst. The kinetic studies showed that the reaction

rate was only related to the toluene pressure rather than oxygen pressure in the feed gas. Thus, we could deduce that the oxygen of catalyst was vital for the toluene combustion. Moreover, it is widely accepted that the oxygen needed for the toluene reaction was those from the palladium oxide species [31,50,51], which was formed by the migration of surface lattice oxygen of zirconium oxide [20]. In order to understand the role of oxygen of catalyst, toluene was passed into a catalyst in the absence of oxygen to detect the reaction mechanism of toluene oxidation process.

Fig. 5A and C show the *in situ*-DRIFTS spectrum of Pd/m-ZrO<sub>2</sub> and Pd/t-ZrO<sub>2</sub> in the presence of 1000 ppm toluene as a function of time. The bands at 3689, 3587 and 3566 cm<sup>-1</sup> were attributed to the tensile vibration peaks of hydroxyl groups on the surface of the catalyst [28,38, 52]. The peaks at 1688, 1733, 1653 and 1648 cm<sup>-1</sup> were assigned to C=O tensile vibrations of aldehydes [38]. The peak at 1260 cm<sup>-1</sup> was associated with the C–O tensile vibration peak of benzyl alcohol group [53,54]. The peaks at 1496 and 1508 cm<sup>-1</sup> were attributed to the typical skeleton (C=C) vibration of the toluene aromatic ring [55]. The peaks of 1395, 1338, and 1540 cm<sup>-1</sup> were ascribed to the typical vibration of carboxylic acid species (symmetric stretch vibration and asymmetric stretch vibration) [5,56], and the peak of 1400 cm<sup>-1</sup> was considered to be the typical peak of mono-dentate carboxylate [57,61]. The bands at 1363 and 1473 cm<sup>-1</sup> were assigned to the (CH<sup>-</sup>) symmetric and asymmetric deformation vibrations of the methyl (CH<sub>3</sub>) group [6,58,59]. The

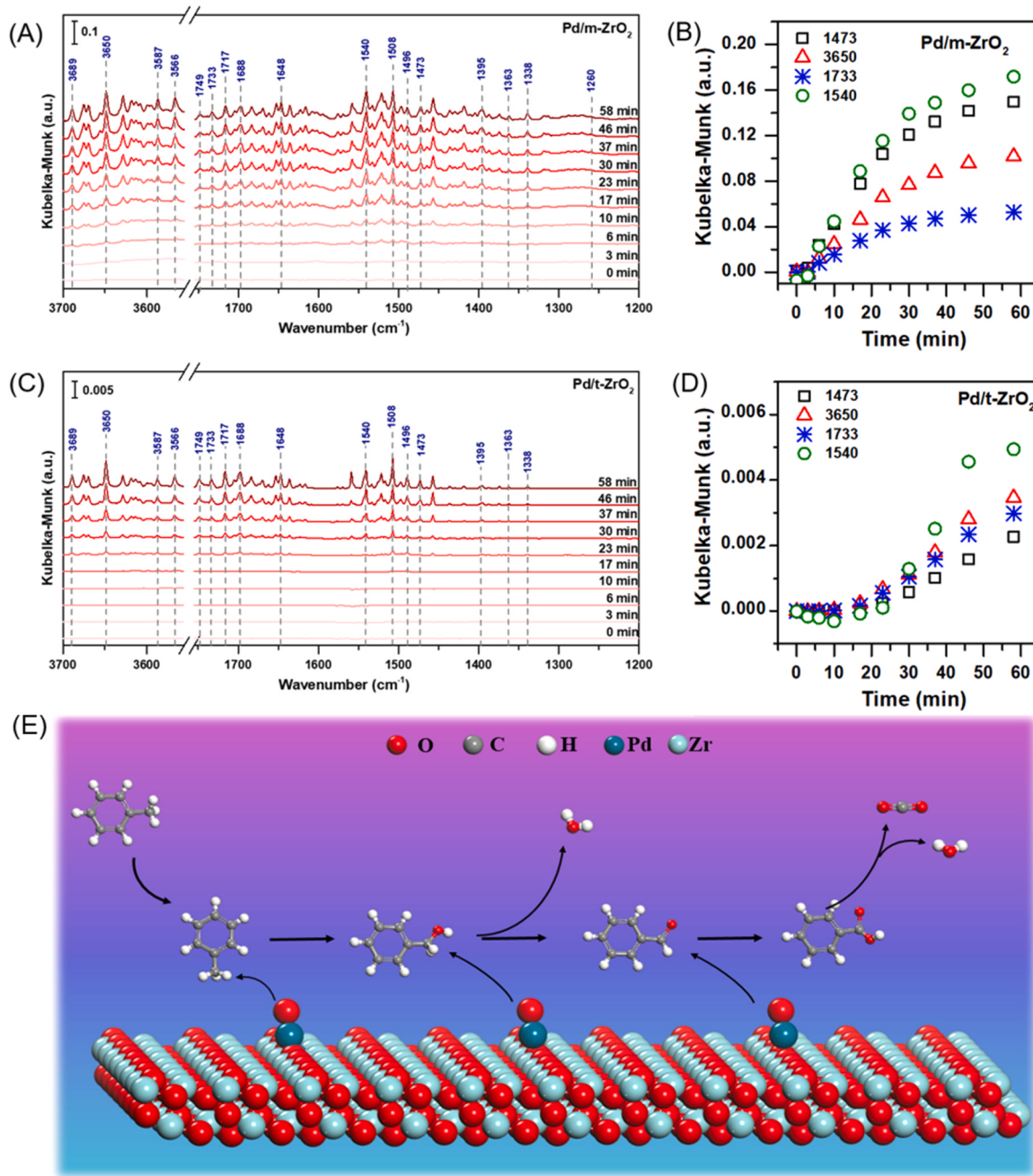


**Fig. 5.** Time-resolved DRIFT spectra showing accumulation of surface species over Pd/m-ZrO<sub>2</sub> (A) and Pd/t-ZrO<sub>2</sub> (C) catalyst; The IR band heights of the surface key species over Pd/m-ZrO<sub>2</sub> (B) and Pd/t-ZrO<sub>2</sub> (D) catalyst; reaction pathway of catalytic combustion of toluene on Pd/ZrO<sub>2</sub> (E).

bands of 1749 and 1717 cm<sup>-1</sup> were associated with the C—O—C characteristic peaks of anhydride species [19,55,60] and the C=O vibration peaks of ketones, respectively. All these intermediate species and corresponding peak positions are shown in Table 2. For both Pd/ZrO<sub>2</sub> catalysts, the characteristic peaks of toluene (1508 cm<sup>-1</sup>) and benzyl alcohol (3650 cm<sup>-1</sup>) first appeared, indicating that toluene was initially adsorbed on the surface of the catalyst and oxidized to benzyl alcohol. Then the characteristic peak of benzaldehyde (1733 cm<sup>-1</sup>) and benzoic acid (1540 cm<sup>-1</sup>) gradually appeared indicating that benzyl alcohol was further oxidized to benzaldehyde, regenerated into benzoic acid, and finally turned into CO<sub>2</sub> and water. It should be noted that the intensity of adsorbed species of Pd/m-ZrO<sub>2</sub> was ca. 20 times than that of Pd/t-ZrO<sub>2</sub>, illustrating more adsorption of toluene on Pd/m-ZrO<sub>2</sub> than Pd/t-ZrO<sub>2</sub>, which was consistent with the kinetic studies. Moreover, from the intensity of IR species, the rate-determining step in the whole reaction

**Table 2**

Assignment of DRIFTS bands for the adsorbed species [5,28,38,52–61].

Vibrations (cm <sup>-1</sup> )	Assignment
3689, 3587, 3566	O—H stretching vibration peaks of surface hydroxyl groups
3650, 1260	O—H vibrational peaks and C—O stretching vibrational peaks of benzyl alcohol groups
1688, 1733, 1653, 1648	C=O stretching vibration peak of benzaldehyde
1496, 1508	C=C stretching vibration peak of benzene ring skeleton
1338, 1395, 1400, 1540	Correlation peaks for typical benzoic acid species
1363, 1473	(CH <sub>3</sub> ) Symmetric and Asymmetric Stretching Vibrations of the CH <sub>3</sub> -Group
1717	C=O vibration peaks of ketones
1749	C—O—C characteristic peaks of anhydride species

could be deduced. The characteristic peak of each species was related to its rate of production and consumption. By analyzing the intensity with respect to time, it was found that the intensity of the characteristic peak of benzaldehyde increased gradually and plateaued at ca. 40 min, which indicated that the oxidation rate of benzyl alcohol to benzaldehyde was equal to that of benzaldehyde to benzoic acid. However, the strength of the benzoic acid characteristic peak increased steadily at first and then increased gradually even at 60 min, suggesting that the consumption rate of benzoic acid was lower than the production rate. To sum up, the oxidative decomposition of benzoic acid may be the rate-controlling step in the catalytic toluene oxidation. Similar results were also observed by Li et al. [6]. Based on the *In-situ* DRIFTS results, the oxidation process of toluene is shown in Fig. 5E. At the first step, toluene molecules were adsorbed on the surface of the catalyst, and the active PdO species on the surface reacted with the adsorbed toluene to produce benzyl alcohol. It was then oxidized by PdO to generate benzaldehyde, which was further oxidized to produce benzoic acid and finally converted into CO<sub>2</sub> and H<sub>2</sub>O.

### 3.5. A DFT study for reactivity of Pd–O on Pd/ZrO<sub>2</sub>

Previous results, i.e., kinetic studies, XPS and H<sub>2</sub>-TPR, showed that the oxygen of the catalyst was vital for toluene combustion. Therefore, theoretical models of Pd/ZrO<sub>2</sub> catalysts were established to study the properties of Pd–O bonds via calculating the desorption energy ( $E_{\text{des}}$ ) and the partial density of states (PDOS) of O upon O–Pd/ZrO<sub>2</sub> [62]. The optimized structures of m-ZrO<sub>2</sub> (111) and t-ZrO<sub>2</sub> (101) surface were used to construct the O–Pd/ZrO<sub>2</sub> system (Fig. 6A). It was calculated that the maximum desorption energies of O atoms in O–Pd/m-ZrO<sub>2</sub> and O–P/t-ZrO<sub>2</sub> were 1.46 and 0.53 eV, respectively (Table 3), implying that Pd–O species on the surface of t-ZrO<sub>2</sub> were more reducible, which was consistent with the experimental results. PDOS of the 2 s and 2p orbitals of O upon Pd/m-ZrO<sub>2</sub> and Pd/t-ZrO<sub>2</sub> (Fig. 6B) illustrated that electron density near the Fermi level of O atom upon Pd/t-ZrO<sub>2</sub> was higher. The energy-weighted average  $\epsilon$  (p-band center) [42,63] of the active O adsorbed on Pd/t-ZrO<sub>2</sub> was -3.03 eV, while the p-band center  $\epsilon$  of the active O adsorbed on Pd/m-ZrO<sub>2</sub> was -3.26 eV, implying that the active O upon Pd/t-ZrO<sub>2</sub> was more unstable than Pd/m-ZrO<sub>2</sub>. These results were in agreement with the electron transfer clarified by XPS and CO-DRIFTS. All these provided a basic understanding of O–Pd on Pd/ZrO<sub>2</sub> via the desorption energy and PDOS.

## 4. Conclusions

In this work, the effect of ZrO<sub>2</sub> crystalline phases on Pd/ZrO<sub>2</sub> catalysts was studied for toluene combustion. Pd/t-ZrO<sub>2</sub> showed excellent

**Table 3**

Total energies of systems used to calculate the oxygen desorption energy ( $E_{\text{des}}$ ) upon the m-ZrO<sub>2</sub>(111)-(1 × 1) surface and t-ZrO<sub>2</sub>(101)-(2 × 1) surface.

Surface	Adsorption site	$E(\text{Pd}+\text{m-ZrO}_2)$ (eV)	$E(\text{O}+\text{Pd}+\text{m-ZrO}_2)$ (eV)	$E(\text{O})$ (eV)	$E_{\text{des}}$ (eV)
m-ZrO <sub>2</sub> (111)-(1 × 1)	1	-228.34	-233.89	-4.93	0.62
	2	-227.50	-233.89	-	1.46
	3	-228.36	-233.92	-	0.63
	4	-227.93	-233.38	-	0.52
t-ZrO <sub>2</sub> (101)-(2 × 1)	1'	-229.86	-235.32	-4.93	0.53
	2'	-229.86	-235.14	-	0.35
	3'	-229.81	-234.90	-	0.16
	4'	-229.50	-234.78	-	0.35

catalytic performance at low concentration of toluene, while Pd/m-ZrO<sub>2</sub> exhibited superior catalytic performance at high toluene concentration. Kinetic studies showed that the reaction order of toluene on Pd/t-ZrO<sub>2</sub> was 0 and that on Pd/m-ZrO<sub>2</sub> was 2. Meanwhile, the reaction order of oxygen on both Pd/ZrO<sub>2</sub> was 0. H<sub>2</sub>-TPR, XPS and OSC indicated that t-ZrO<sub>2</sub> contributed to the formation of highly active PdO species, while m-ZrO<sub>2</sub> was beneficial for the higher content of PdO species. The catalytic activity was correlated with comprehensive effect between the amount and chemical properties of PdO on the surface of the catalysts. DFT results demonstrated that electron density near the Fermi level and p-band center of O atom on Pd/t-ZrO<sub>2</sub> were higher than that of Pd/m-ZrO<sub>2</sub>, thus weakening the Pd–O bond. *In situ*-DRIFTS results revealed the reaction path of toluene oxidation: gaseous toluene was firstly adsorbed on the surface of the catalyst and then subsequently oxidized to benzyl alcohol, benzaldehyde, benzoic acid, and finally completely oxidized to CO<sub>2</sub> and H<sub>2</sub>O. These results revealed the influence of the crystal effect of the support on the catalytic combustion reaction via the combination of kinetic studies, DRIFTS and DFT theory in depth, providing a guideline for the design and development of high performance catalysts for VOCs combustion.

### CRediT authorship contribution statement

**Decun Luo:** Formal analysis, Investigation, Writing – original draft, Visualization. **Ziyu Tang:** Visualization, Data curation. **Xiyang Yu:** Visualization. **Tao Zhang:** Data curation, Validation. **Chun-Ran Chang:** Supervision, Funding acquisition. **Zhun Hu:** Project administration, Funding acquisition, Supervision, Writing - review & editing.

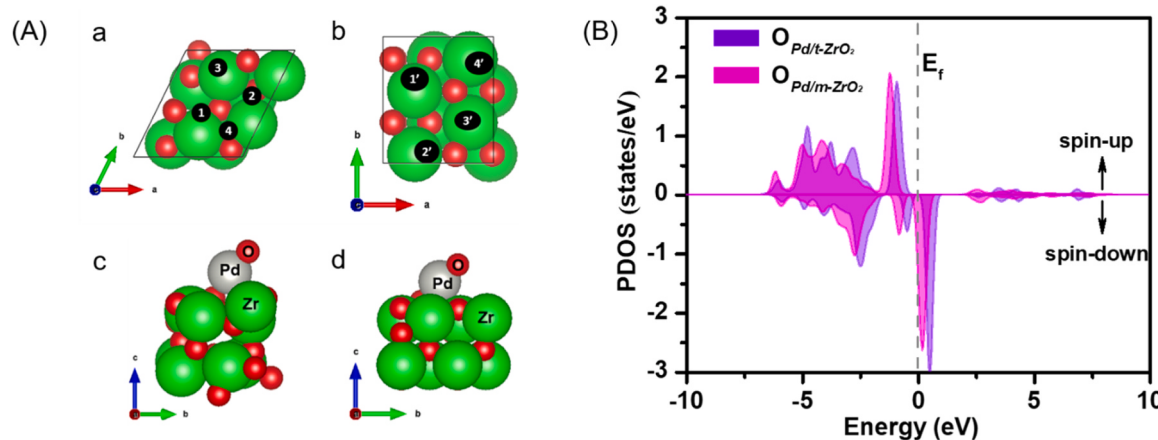


**Fig. 6.** (A) Adsorption sites Pd–O species upon m-ZrO<sub>2</sub> (a) and t-ZrO<sub>2</sub> (b), and the modes of Pd/m-ZrO<sub>2</sub> (c) and Pd/t-ZrO<sub>2</sub> (d). (B) PDOS of the 2s and 2p orbitals of O upon Pd/m-ZrO<sub>2</sub> and Pd/t-ZrO<sub>2</sub>.

## Declaration of Competing Interest

The authors declare that they have no known competing financial interests or personal relationships that could have appeared to influence the work reported in this paper.

## Data Availability

The data that has been used is confidential.

## Acknowledgments

The authors acknowledge the financial support from the National Natural Science Foundation of China (22078257, 22038011 and 21802107), the Fundamental Research Funds for the Central Universities (xjh012020015), and the Young Talent Support Plan of Shaanxi Province. Dr. Zhun Hu acknowledges Chaoyang Wei in the preparation of support.

## Appendix A. Supporting information

Supplementary data associated with this article can be found in the online version at doi:[10.1016/j.apcatb.2023.123117](https://doi.org/10.1016/j.apcatb.2023.123117).

## References

- [1] J. Jeong, K. Sekiguchi, W. Lee, K. Sakamoto, Photodegradation of gaseous volatile organic compounds (VOCs) using TiO<sub>2</sub> photoirradiated by an ozone-producing UV lamp: decomposition characteristics, identification of by-products and water-soluble organic intermediates, *J. Photochem. Photobiol. A: Chem.* 169 (2005) 279–287.
- [2] M.S. Kamal, S.A. Razzak, M.M. Hossain, Catalytic oxidation of volatile organic compounds (VOCs) – a review, *Atmos. Environ.* 140 (2016) 117–134.
- [3] H. Liu, J. Yang, Y. Jia, Z. Wang, M. Jiang, K. Shen, H. Zhao, Y. Guo, Y. Guo, L. Wang, S. Dai, W. Zhan, Significant improvement of catalytic performance for chlorinated volatile organic compound oxidation over RuO<sub>x</sub> supported on acid-etched Co<sub>3</sub>O<sub>4</sub>, *Environ. Sci. Technol.* 55 (2021) 10734–10743.
- [4] Y. Yang, G. Wang, P. Zheng, F. Dang, J. Han, Carbon deposits during catalytic combustion of toluene on Pd–Pt-based catalysts, *Catal. Sci. Technol.* 10 (2020) 2452–2461.
- [5] M.B. S. H. Idriss, The reaction of propylene to propylene-oxide on CeO<sub>2</sub>: An FTIR spectroscopy and temperature programmed desorption study, *J. Chem. Phys.* 152 (2020), 044712.
- [6] S. Mo, Q. Zhang, J. Li, Y. Sun, Q. Ren, S. Zou, Q. Zhang, J. Lu, M. Fu, D. Mo, J. Wu, H. Huang, D. Ye, Highly efficient mesoporous MnO<sub>2</sub> catalysts for the total toluene oxidation: Oxygen-Vacancy defect engineering and involved intermediates using in situ DRIFTS, *Appl. Catal. B: Environ.* 264 (2020), 118464.
- [7] Z. Hu, X. Yong, D. Li, R.T. Yang, Synergism between palladium and nickel on Pd-Ni/TiO<sub>2</sub> for H<sub>2</sub>-SCR: A transient DRIFTS study, *J. Catal.* 381 (2020) 204–214.
- [8] Q. Zhou, C. Zhou, Y. Zhou, W. Hong, S. Zou, X.-Q. Gong, J. Liu, L. Xiao, J. Fan, More than oxygen vacancies: a collective crystal-plane effect of CeO<sub>2</sub> in gas-phase selective oxidation of benzyl alcohol, *Catal. Sci. Technol.* 9 (2019) 2960–2967.
- [9] C. He, X. Zhang, S. Gao, J. Chen, Z. Hao, Nanometric Pd-confined mesoporous silica as high-efficient catalyst for toluene low temperature removal: effects of support morphology and textural property, *J. Ind. Eng. Chem.* 18 (2012) 1598–1605.
- [10] C. He, Q. Li, P. Li, Y. Wang, X. Zhang, J. Cheng, Z. Hao, Templatized silica with increased surface area and expanded microporosity: synthesis, characterization, and catalytic application, *Chem. Eng. J.* 162 (2010) 901–909.
- [11] N. Qiao, Y. Li, N. Li, X. Zhang, J. Cheng, Z. Hao, High performance Pd catalysts supported on bimodal mesopore silica for the catalytic oxidation of toluene, *Chin. J. Catal.* 36 (2015) 1686–1693.
- [12] Y. Li, Y. Li, Q. Yu, L. Yu, The catalytic oxidation of toluene over Pd-based FeCrAl wire mesh monolithic catalysts prepared by electroless plating method, *Catal. Commun.* 29 (2012) 127–131.
- [13] S. Xie, J. Deng, S. Zang, H. Yang, G. Guo, H. Arandiyani, H. Dai, Au-Pd/3DOM Co<sub>3</sub>O<sub>4</sub>: highly active and stable nanocatalysts for toluene oxidation, *J. Catal.* 322 (2015) 38–48.
- [14] H. Yang, J. Deng, Y. Liu, S. Xie, Z. Wu, H. Dai, Preparation and catalytic performance of Ag, Au, Pd or Pt nanoparticles supported on 3DOM CeO<sub>2</sub>-Al<sub>2</sub>O<sub>3</sub> for toluene oxidation, *J. Mol. Catal. A: Chem.* 414 (2016) 9–18.
- [15] S. Zhao, K. Li, S. Jiang, J. Li, Pd–Co based spinel oxides derived from pd nanoparticles immobilized on layered double hydroxides for toluene combustion, *Appl. Catal. B: Environ.* 181 (2016) 236–248.
- [16] C. Hu, Catalytic combustion kinetics of acetone and toluene over Cu<sub>0.13</sub>Ce<sub>0.87</sub>O<sub>y</sub> catalyst, *Chem. Eng. J.* 168 (2011) 1185–1192.
- [17] C. He, L. Xu, L. Yue, Y. Chen, J. Chen, Z. Hao, Supported nanometric Pd hierarchical catalysts for efficient toluene removal: catalyst characterization and activity elucidation, *Ind. Eng. Chem. Res.* 51 (2012) 7211–7222.
- [18] Z. Yang, H. Yi, X. Tang, S. Zhao, Y. Huang, X. Xie, L. Song, Y. Zhang, Study of reaction mechanism based on further promotion of low temperature degradation of toluene using nano-CeO<sub>2</sub>/Co<sub>3</sub>O<sub>4</sub> under microwave radiation for cleaner production in spraying processing, *J. Hazard. Mater.* 373 (2019) 321–334.
- [19] X. Yang, X. Yu, M. Lin, X. Ma, M. Ge, Enhancement effect of acid treatment on Mn<sub>2</sub>O<sub>3</sub> catalyst for toluene oxidation, *Catal. Today* 327 (2019) 254–261.
- [20] C. Jiang, H. Wang, S. Lin, F. Ma, Y. Wang, H. Ji, Low-temperature photothermal catalytic oxidation of toluene on a core/shell SiO<sub>2</sub>@Pt@ZrO<sub>2</sub> nanostructure, *Ind. Eng. Chem. Res.* 58 (2019) 16450–16458.
- [21] W. Yang, D. Li, D. Xu, X. Wang, Effect of CeO<sub>2</sub> preparation method and Cu loading on CuO/CeO<sub>2</sub> catalysts for methane combustion, *J. Nat. Gas Chem.* 18 (2009) 458–466.
- [22] X. Feng, J. Guo, X. Wen, M. Xu, Y. Chu, S. Yuan, Enhancing performance of Co/CeO<sub>2</sub> catalyst by Sr doping for catalytic combustion of toluene, *Appl. Surf. Sci.* 445 (2018) 145–153.
- [23] Z. Feng, Q. Ren, R. Peng, S. Mo, M. Zhang, M. Fu, L. Chen, D. Ye, Effect of CeO<sub>2</sub> morphologies on toluene catalytic combustion, *Catal. Today* 332 (2019) 177–182.
- [24] F. Hu, J. Chen, Y. Peng, H. Song, K. Li, J. Li, Novel nanowire self-assembled hierarchical CeO<sub>2</sub> microspheres for low temperature toluene catalytic combustion, *Chem. Eng. J.* 331 (2018) 425–434.
- [25] F. Yin, S. Ji, P. Wu, F. Zhao, C. Li, Deactivation behavior of Pd-based SBA-15 mesoporous silica catalysts for the catalytic combustion of methane, *J. Catal.* 257 (2008) 108–116.
- [26] Z. Ye, J.M. Giraudon, N. Nuns, P. Simon, N. De Geyter, R. Morent, J.F. Lamonié, Influence of the preparation method on the activity of copper-manganese oxides for toluene total oxidation, *Appl. Catal. B: Environ.* 223 (2018) 154–166.
- [27] A. Baylet, S. Royer, R. Marecot, J.M. Tatiboutet, D. Duprez, High catalytic activity and stability of Pd doped hexaaluminates catalysts for the CH<sub>4</sub> catalytic combustion, *Appl. Catal. B-Environ.* 77 (2008) 237–247.
- [28] S. Zhao, F. Hu, J. Li, Hierarchical core-shell Al<sub>2</sub>O<sub>3</sub>@Pd-CoAlO microspheres for low-temperature toluene combustion, *ACS Catal.* 6 (2016) 3433–3441.
- [29] F. Bi, X. Zhang, S. Xiang, Y. Wang, Effect of Pd loading on ZrO<sub>2</sub> support resulting from pyrolysis of UiO-66: application to CO oxidation, *J. Colloid Interface Sci.* 573 (2020) 11–20.
- [30] J. Du, H. Li, C. Wang, A. Zhang, Y. Zhao, Y. Luo, Improved catalytic activity over P-doped ceria-zirconia-alumina supported palladium catalysts for methane oxidation, *Catal. Commun.* 141 (2020), 106012.
- [31] E. Hong, C. Kim, D.-H. Lim, H.-J. Cho, C.-H. Shin, Catalytic methane combustion over Pd/ZrO<sub>2</sub> catalysts: effects of crystalline structure and textural properties, *Appl. Catal. B: Environ.* 232 (2018) 544–552.
- [32] J.B. Miller, M. Malapure, Pd catalysts for total oxidation of methane: Support effects, *Appl. Catal. A: Gen.* 495 (2015) 54–62.
- [33] J.-H. Park, J.H. Cho, Y.J. Kim, E.S. Kim, H.S. Han, C.-H. Shin, Hydrothermal stability of Pd/ZrO<sub>2</sub> catalysts for high temperature methane combustion, *Appl. Catal. B: Environ.* 160–161 (2014) 135–143.
- [34] Y. Shao, Z. Xu, H. Wan, Chen, F. Liu, L. Li, S. Zheng, Influence of ZrO<sub>2</sub> properties on catalytic hydrodechlorination of chlorobenzene over Pd/ZrO<sub>2</sub> catalysts, *J. Hazard. Mater.* 179 (2010) 135–140.
- [35] R. Burch, F.J. Urbano, P.K. Loader, Methane combustion over Palladium catalysts - the effect of carbon-dioxide and water on activity, *Appl. Catal. A-Gen.* 123 (1995) 173–184.
- [36] P. Araya, S. Guerrero, J. Robertson, F.J. Gracia, Methane combustion over Pd/SiO<sub>2</sub> catalysts with different degrees of hydrophobicity, *Appl. Catal. A-Gen.* 283 (2005) 225–233.
- [37] J. Zhao, B. Wang, W. Yu, Z. Li, Y. Xu, X. Ma, Carbon-limited conversion of molybdenum carbide into curved ultrasmall monolayer molybdenum disulfide under effects of ZrO<sub>2</sub> crystal phases for efficient sulfur-resistant methanation, *ChemCatChem* 11 (2019) 3046–3053.
- [38] R. Mi, D. Li, Z. Hu, R.T. Yang, Morphology effects of CeO<sub>2</sub> nanomaterials on the catalytic combustion of toluene: a combined kinetics and diffuse reflectance infrared fourier transform spectroscopy study, *ACS Catal.* 11 (2021) 7876–7889.
- [39] G. Kresse, J. Furthmüller, Efficiency of ab-initio total energy calculations for metals and semiconductors using a plane-wave basis set, *Comput. Mater. Sci.* 6 (1996) 15–50.
- [40] G. Kresse, D. Joubert, From ultrasoft pseudopotentials to the projector augmented-wave method, *Phys. Rev. B* 59 (1999) 1758–1775.
- [41] C.A. Muller, M. Maciejewski, R.A. Koeppl, A. Baiker, Combustion of methane over palladium/zirconia: effect of Pd-particle size and role of lattice oxygen, *Catal. Today* 47 (1999) 245–252.
- [42] R. Wischert, P. Laurent, C. Copéret, F. Delbecq, P. Sautet, γ-Alumina: the essential and unexpected role of water for the structure, stability, and reactivity of "defect" sites, *J. Am. Chem. Soc.* 134 (2012) 14430–14449.
- [43] Z. Tang, T. Zhang, D. Luo, Y. Wang, Z. Hu, R.T. Yang, Catalytic combustion of methane: from mechanism and materials properties to catalytic performance, *ACS Catal.* 12 (2022) 13457–13474.
- [44] C. He, J. Cheng, X. Zhang, M. Douthwaite, S. Pattisson, Z. Hao, Recent advances in the catalytic oxidation of volatile organic compounds: a review based on pollutant sorts and sources, *Chem. Rev.* 119 (2019) 4471–4568.
- [45] A.P. Jurka Batista, Djordje Mandrin, Monika Jenko, Vincent Martin, XPS and TPR examinations of γ-alumina-supported Pd–Cu catalysts, *Appl. Catal. A-Gen.* 206 (2001) 113–124.
- [46] Y. Shao, Z. Xu, H. Wan, H. Chen, F. Liu, L. Li, S. Zheng, Influence of ZrO<sub>2</sub> properties on catalytic hydrodechlorination of chlorobenzene over Pd/ZrO<sub>2</sub> catalysts, *J. Hazard. Mater.* 179 (2010) 135–140.

- [47] Y. Wu, J. Chen, W. Hu, K. Zhao, P. Qu, P. Shen, M. Zhao, L. Zhong, Y. Chen, Phase transformation and oxygen vacancies in Pd/ZrO<sub>2</sub> for complete methane oxidation under lean conditions, *J. Catal.* 377 (2019) 565–576.
- [48] Z. Zhang, L. Zhang, M.J. Hulsey, N. Yan, Zirconia phase effect in Pd/ZrO<sub>2</sub> catalyzed CO<sub>2</sub> hydrogenation into formate, *Mol. Catal.* 475 (2019), 110461.
- [49] H. Jeong, J. Bae, J.W. Han, H. Lee, Promoting effects of hydrothermal treatment on the activity and durability of Pd/CeO<sub>2</sub> catalysts for CO oxidation, *ACS Catal.* 7 (2017) 7097–7105.
- [50] X. Auvray, A. Lindholm, M. Milh, L. Olsson, The addition of alkali and alkaline earth metals to Pd/Al<sub>2</sub>O<sub>3</sub> to promote methane combustion: effect of Pd and Ca loading, *Catal. Today* 299 (2018) 212–218.
- [51] A. Toso, S. Colussi, S. Padigapati, C. de Leitenburg, A. Trovarelli, High stability and activity of solution combustion synthesized Pd-based catalysts for methane combustion in presence of water, *Appl. Catal. B: Environ.* 230 (2018) 237–245.
- [52] J.-J. Li, E.-Q. Yu, S.-C. Cai, X. Chen, J. Chen, H.-P. Jia, Y.-J. Xu, Noble metal free, CeO<sub>2</sub>/LaMnO<sub>3</sub> hybrid achieving efficient photo-thermal catalytic decomposition of volatile organic compounds under IR light, *Appl. Catal. B: Environ.* 240 (2019) 141–152.
- [53] J. Du, Z. Qu, C. Dong, L. Song, Y. Qin, N. Huang, Low-temperature abatement of toluene over Mn-Ce oxides catalysts synthesized by a modified hydrothermal approach, *Appl. Surf. Sci.* 433 (2018) 1025–1035.
- [54] Q. Zhang, S. Mo, J. Li, Y. Sun, M. Zhang, P. Chen, M. Fu, J. Wu, L. Chen, D. Ye, In situ DRIFT spectroscopy insights into the reaction mechanism of CO and toluene co-oxidation over Pt-based catalysts, *Catal. Sci. Technol.* 9 (2019) 4538–4551.
- [55] J. Li, D.-f Lu, Z. Zhang, Q. Liu, Z.-m Qi, Hierarchical mesoporous silica film modified near infrared SPR sensor with high sensitivities to small and large molecules, *Sens. Actuators B-Chem.* 203 (2014) 690–696.
- [56] A. Lu, H. Sun, N. Zhang, L. Che, S. Shan, J. Luo, J. Zheng, L. Yang, D.-L. Peng, C.-J. Zhong, B. Chen, Surface partial-charge-tuned enhancement of catalytic activity of platinum nanocatalysts for toluene oxidation, *ACS Catal.* 9 (2019) 7431–7442.
- [57] K. Li, K. Liu, H. Ni, B. Guan, R. Zhan, Z. Huang, H. Lin, Electric field promoted ultra-lean methane oxidation over Pd-Ce-Zr catalysts at low temperature, *Mol. Catal.* 459 (2018) 78–88.
- [58] C. Zhang, C. Wang, H. Huang, K. Zeng, Z. Wang, H.-p Jia, X. Li, Insights into the size and structural effects of zeolitic supports on gaseous toluene oxidation over MnO<sub>x</sub>/HZSM-5 catalysts, *Appl. Surf. Sci.* 486 (2019) 108–120.
- [59] M.D. Hernandez-Alonso, I. Tejedor-Tejedor, J.M. Coronado, M.A. Anderson, Operando FTIR study of the photocatalytic oxidation of methylcyclohexane and toluene in air over TiO<sub>2</sub>-ZrO<sub>2</sub> thin films: influence of the aromaticity of the target molecule on deactivation, *Appl. Catal. B: Environ.* 101 (2011) 283–293.
- [60] F. Rainone, D.A. Bulushev, L. Kiwi-Minsker, A. Renken, DRIFTS and transient-response study of vanadia/titania catalysts during toluene partial oxidation, *Phys. Chem. Chem. Phys.* 5 (2003) 4445–4449.
- [61] L. Ma, C.Y. Seo, X. Chen, K. Sun, J.W. Schwank, Indium-doped Co<sub>3</sub>O<sub>4</sub> nanorods for catalytic oxidation of CO and C<sub>3</sub>H<sub>6</sub> towards diesel exhaust, *Appl. Catal. B: Environ.* 222 (2018) 44–58.
- [62] X.-Y. Xu, S. Lin, H. Xu, H. Guo, C. Zhao, Mechanistic insights into the CO oxidation reaction catalyzed by P-coordinated metal-doped graphene: the roles of phosphorus and metal atom, *Appl. Surf. Sci.* 556 (2021), 149776.
- [63] S. Zhang, Z. Xia, Y. Zou, F. Cao, Y. Liu, Y. Ma, Y. Qu, Interfacial frustrated lewis pairs of CeO<sub>2</sub> activate CO<sub>2</sub> for selective tandem transformation of olefins and CO<sub>2</sub> into cyclic carbonates, *J. Am. Chem. Soc.* 141 (2019) 11353–11357.